



# Ni-doped $\text{Bi}_{0.5}\text{Sb}_{1.5}\text{Te}_3$ single crystal: a potential functional material for thermoelectricity, topological insulator, and optoelectronics

Sahiba Bano<sup>1,2</sup> · Bal Govind<sup>1,2</sup> · Ashish Kumar<sup>1,2</sup> · D. K. Misra<sup>1</sup>

Received: 13 June 2020 / Accepted: 29 July 2020 / Published online: 8 August 2020  
© Springer Science+Business Media, LLC, part of Springer Nature 2020

## Abstract

We report the growth of Ni-doped  $\text{Bi}_{0.5}\text{Sb}_{1.35}\text{Ni}_{0.15}\text{Te}_3$  single crystal via the self-flux method. The crystalline nature of a grown single crystal was confirmed by the X-ray diffraction technique (XRD). Interestingly, the XRD pattern shows a sharp reflections of  $\langle 0\ 0\ 1 \rangle$  type of planes, revealing the growth of the crystal in *c*-direction. The grown single crystal was subjected for measurement of field dependence magnetization at 300 K and temperature-dependent magnetic moment. The electronic transport property of bulk single crystal was also carried out in a wide range of temperatures from 150 to 450 K. Reasonably large electrical conductivity  $\sigma \sim 1584$  S/cm at room temperature was observed which shows  $\sim 400\%$  enhancement in  $\sigma$  than the electrical conductivity of bare  $\text{Bi}_{0.5}\text{Sb}_{1.5}\text{Te}_3$  single crystal (400 S/cm at 300 K). This enhanced electrical conductivity results to significant power factor  $\sim 1.68 \times 10^{-3}$  W/m  $\text{K}^2$  at 300K which is 163% larger than that of bare  $\text{Bi}_{0.5}\text{Sb}_{1.5}\text{Te}_3$  single crystal ( $6.45 \times 10^{-4}$  W/m  $\text{K}^2$ ). Magnetic properties of a single crystal of  $\text{Bi}_{0.5}\text{Sb}_{1.35}\text{Ni}_{0.15}\text{Te}_3$  reveal ferromagnetic behavior at 300 K. The photoluminescence (PL) behavior of  $\text{Bi}_{0.5}\text{Sb}_{1.35}\text{Ni}_{0.15}\text{Te}_3$  single-crystal was also scrutinized. The PL spectra of  $\text{Bi}_{0.5}\text{Sb}_{1.35}\text{Ni}_{0.15}\text{Te}_3$  single crystal shows the strong red emission peak in the visible region from 600 to 690 nm upon excitation at 375 nm wavelength, which corresponds to the optical bandgap of 2.1 eV.

## 1 Introduction

Research on thermoelectric materials is becoming an intriguing topic since the past decades due to owing their demand for power generation and cooling applications. The performance of thermoelectric materials is elucidated by the dimensionless figure of merit,  $ZT = (\alpha^2\sigma/\kappa) T$  where  $\sigma$ ,  $\alpha$ , and  $\kappa$  are the electrical conductivity, Seebeck coefficient, and total thermal conductivity, respectively, at the absolute temperature (*T*) [1]. Improving the power factor,  $\alpha^2\sigma$ , seems to be an excellent approach to enhance the efficiency of thermoelectric materials. There are different approaches such that multiple band convergences [2–4], tuning the bandgap [5–7], modulation of carrier scattering mechanisms [8, 9] and inducing modulated doping to enhance power factor of materials. Recently, the strategy of doping of magnetic ion has been investigated to escalate the thermopower [10–13].

There has also been the efficacy of magnetic doping on the thermoelectric properties of antiferromagnetic  $\text{CuFeS}_2$  chalcopyrites [10, 11, and 13] and  $\text{CuGaTe}_2$  chalcopyrite [12].

$\text{Bi}_2\text{Te}_3$  thermoelectric materials have been investigated extensively due to its excellent thermoelectric properties at room temperature.  $\text{Bi}_2\text{Te}_3$  has a rhombohedral structure with space group  $R\bar{3}m$  (#166). It exhibits a layered structure assembled in three quintuple layers of Te(1)-Bi-Te(2)-Bi-Te(1).  $\text{Bi}_2\text{Te}_3$  is also one of the well-known 3D topological insulators. It has a large electronic bandgap with a single Dirac-cone-like topologically protected metallic surface. The insulating behavior of this material from the interior and conducting at the surface makes it a potential candidate for optoelectronic applications and tera-hertz applications [14–16].

$\text{Bi}_{0.5}\text{Sb}_{1.5}\text{Te}_3$  is the best-optimized composition so far, which is being used for low-temperature applications [17]. Recently, magnetic dopants, e.g., Cr, Ni, and Mn-doped  $\text{Bi}_2\text{Te}_3$ -based thermoelectric materials, have also been shown as an efficient strategy to achieve high efficiency [18–20]. J. B. et al. [20] reported magnetic doping of Cr in  $\text{Bi}_2\text{Te}_3$  yielding improved efficiency due to magnetic interaction with carriers. Moreover, Mn doping in  $\text{Bi}_{0.5}\text{Sb}_{1.5}\text{Te}_3$  has

✉ D. K. Misra  
misradk@nplindia.org

<sup>1</sup> CSIR-National Physical Laboratory, Dr. K.S. Krishnan Marg, New Delhi 110012, India

<sup>2</sup> Academy of Scientific and Innovative Research (AcSIR), Ghaziabad 201002, India

also been reported to increase carrier concentration yielding to enhanced ZT [18].

Herein, we have taken magnetic dopant Ni to dope in  $\text{Bi}_{0.5}\text{Sb}_{1.5}\text{Te}_3$  and adopted the self-flux method to grow diluted magnetic  $\text{Bi}_{0.5}\text{Sb}_{1.35}\text{Ni}_{0.15}\text{Te}_3$  single crystal. The good crystalline bulk single crystal was obtained, which was confirmed by the XRD diffraction investigation. Further, we have studied electrical transport, magnetic, and optical behavior of the present crystal. Present material exhibits improved electronic transport, enhanced magnetic properties, and significant optical bandgap which are paving a potential candidate for numerous applications in the field of thermoelectric, topological insulators, and optoelectronics.

## 2 Experimental details

The high-purity elements of Bi (99.5%), Sb (99%), Ni (99%), and Te (99.5%) were weighed according to the stoichiometric ratio and mixed well. The mixed powder was sealed in a quartz tube under the pressure of  $10^{-5}$  Torr. The sealed quartz tube is subjected to the electronically

controlled furnace for the solid-state thermal reaction [21, 22]. The furnace temperature was initially set at 900 °C for 7 h 30 min and subsequently was kept on hold at 900 °C for 12 h. Further, furnace temperature was set to decreasing with a rate of 1 °C/ hour till it reaches 600 °C, and then the furnace has switched off for standard cooling to room temperature [23]. Heat treatment and the growth process of single crystal are shown in the schematic diagram in Fig. 1. The powder X-ray diffractometer (PXRD, model: Rigaku Mini Flex II) operated at 30 kV and 20 mA using Cu-K $\alpha$  radiation ( $\lambda = 1.54 \text{ \AA}$ ) in the range 20° to 80° of  $2\theta$  is used to investigate the crystal structure of grown single crystal. The PXRD was performed on the flake of a single crystal and on the powder sample of the same flake of single crystal. Transmission electron microscopy (TEM) was used to determine the microstructure. The magnetic property was examined by vibrating sample magnetometer (VSM; (PPMS-14T, Cryogenics), and Seebeck coefficient and resistivity were measured by ZEM3-L Advance Riko, Japan from 150 to 413 K on a single crystal. Further, its optical emission was measured using the WITec alpha 300R + confocal PL microscope system using a 375 nm diode laser as a source of excitation.

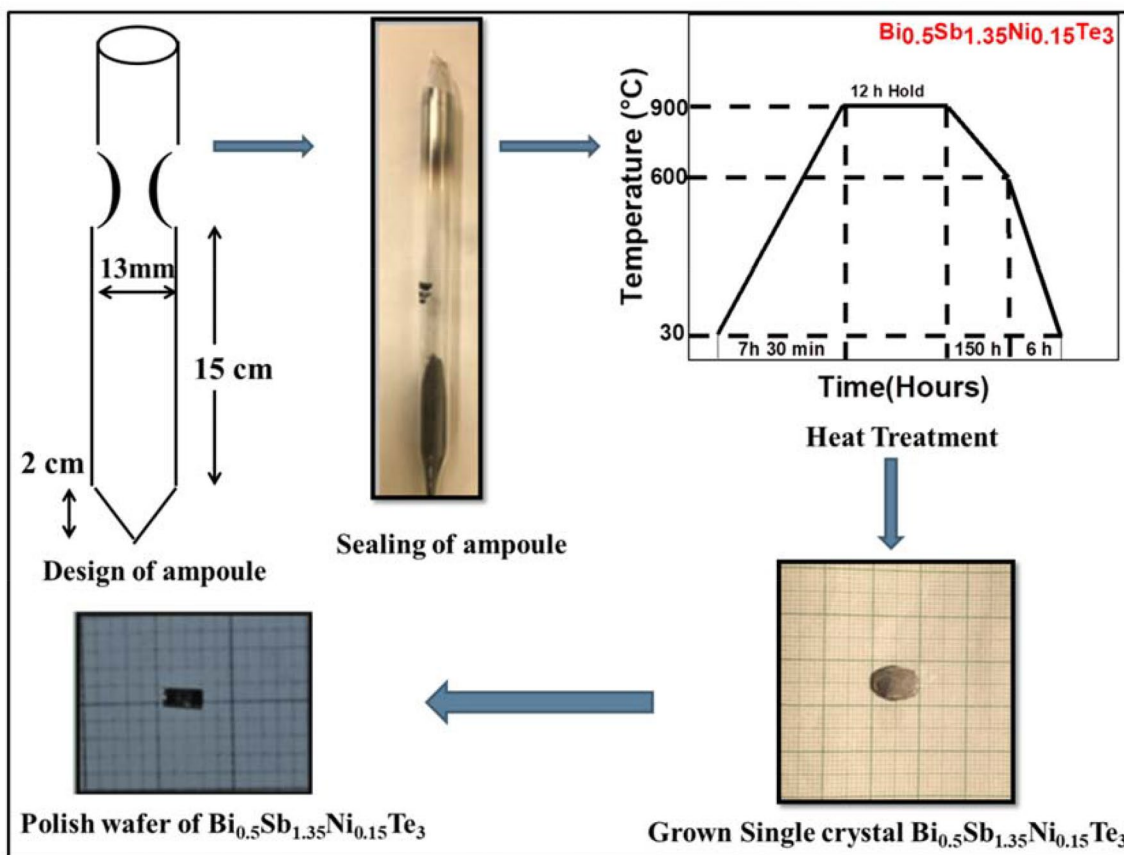


Fig. 1 Stages involved in the growth of single-crystal  $\text{Bi}_{0.5}\text{Sb}_{1.35}\text{Ni}_{0.15}\text{Te}_3$

### 3 Result and discussion

#### 3.1 Structural analysis

##### 3.1.1 XRD investigation

Figure 2a presents the XRD pattern performed on freshly cleaved  $\text{Bi}_{0.5}\text{Sb}_{1.35}\text{Ni}_{0.15}\text{Te}_3$  single crystal in the wide

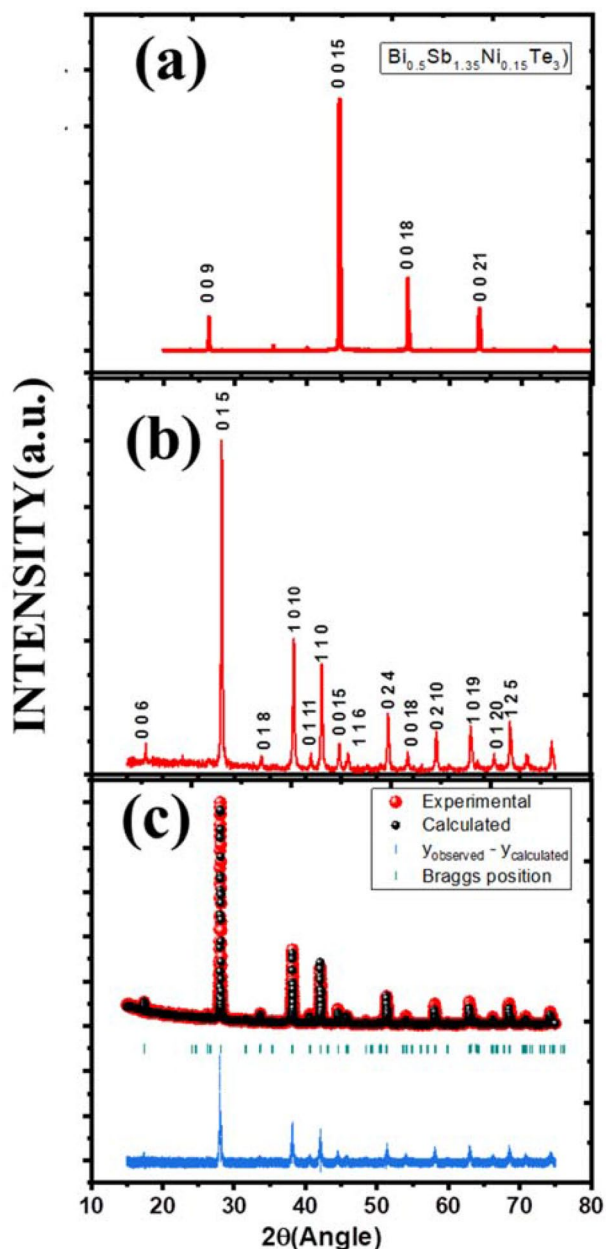


**Fig. 2** a XRD pattern of bulk  $\text{Bi}_{0.5}\text{Sb}_{1.35}\text{Ni}_{0.15}\text{Te}_3$  single crystal. b The powder XRD pattern of crushed powder of  $\text{Bi}_{0.5}\text{Sb}_{1.35}\text{Ni}_{0.15}\text{Te}_3$  and c Rietveld refinement of powder XRD pattern of  $\text{Bi}_{0.5}\text{Sb}_{1.35}\text{Ni}_{0.15}\text{Te}_3$

angular range from  $2\theta = 20^\circ$  to  $80^\circ$ . Interestingly, only sharp reflections of  $\langle 0, 0, l \rangle$  type of planes were observed, revealing a single crystal of  $\text{Bi}_{0.5}\text{Sb}_{1.35}\text{Ni}_{0.15}\text{Te}_3$  which grown in c-direction. Figure 2b presents X-ray diffraction pattern of powder sample obtained from crystal. One can notice that peaks are well indexed with  $\text{Bi}_{0.5}\text{Sb}_{1.5}\text{Te}_3$  phase of rhombohedral structure with space group R-3m (#166). No impurity phase was observed within the detection limit of PXRD. Here, we have estimated the crystallite size of sample  $\text{Bi}_{0.5}\text{Sb}_{1.35}\text{Ni}_{0.15}\text{Te}_3$  using Debye–Scherer formula [24–28] as  $d = \frac{0.89\lambda}{\beta \cos\theta}$  where  $\lambda$  = wavelength of x-ray (0.1542 nm),  $\theta$  = Bragg's diffraction angle, and  $\beta$  = full width at half-maximum.

Here the most intense peaks of  $\text{Bi}_{0.5}\text{Sb}_{1.35}\text{Ni}_{0.15}\text{Te}_3$  in Fig. 2b were used to study the crystalline structure factor and for evaluating crystallite size. The most intense peaks of planes (0 1 5) and (1010) were taken for evaluation of the crystallite structure factor of  $\text{Bi}_{0.5}\text{Sb}_{1.35}\text{Ni}_{0.15}\text{Te}_3$ , which is presented in the Table 1. One can observe from Table 1 that the average crystallite size of  $\text{Bi}_{0.5}\text{Sb}_{1.35}\text{Ni}_{0.15}\text{Te}_3$  was found to be 39.82 nm.

The Rietveld refinement was performed on powder XRD via Full Prof Toolbar Software and is presented in Fig. 2(c). The refinement of the lattice parameter of  $\text{Bi}_{0.5}\text{Sb}_{1.35}\text{Ni}_{0.15}\text{Te}_3$  reveals that Ni doping on the Sb site results in decrease in its value, as shown in Table 2. The decrease in the lattice parameter could be due to the occupation of Ni (~130 pm) to the Sb site (~140 pm) in  $\text{Bi}_{0.5}\text{Sb}_{1.35}\text{Ni}_{0.15}\text{Te}_3$  material.

**Table 1** Parameters for the calculation of the crystallite size of  $\text{Bi}_{0.5}\text{Sb}_{1.35}\text{Ni}_{0.15}\text{Te}_3$

Diffraction Planes	Peak Position ( $2\theta$ in degree)	FWHM ( $\beta$ )	Crystallite Size (nm)	Average size (nm)
(0 1 5)	28.0647	0.1804	44.92	39.82
(1010)	38.1374	0.2396	34.73	

**Table 2** Physical parameters obtained for  $\text{Bi}_{0.5}\text{Sb}_{1.35}\text{Ni}_{0.15}\text{Te}_3$

Physical parameters	$\text{Bi}_{0.5}\text{Sb}_{1.5}\text{Te}_3$	$\text{Bi}_{0.5}\text{Sb}_{1.35}\text{Ni}_{0.15}\text{Te}_3$
$a$ (Å)	4.30 Ref[29]	4.28
$c$ (Å)	30.5 Ref[29]	30.45
$n$ ( $10^{19}/\text{cm}^3$ )	2.3 Ref[30]	3.1

### 3.1.2 Transmission electron microscopy

In order to investigate the microstructure and internal structure of  $\text{Bi}_{0.5}\text{Sb}_{1.35}\text{Ni}_{0.15}\text{Te}_3$  crystal, transmission electron microscopy (TEM) was performed. The bright-field TEM image of  $\text{Bi}_{0.5}\text{Sb}_{1.35}\text{Ni}_{0.15}\text{Te}_3$  presented in Fig. 3a reveals a well-oriented crystal with a layered structure. The high-resolution TEM obtained from the same sample is presented in Fig. 3b with a SAED (Inset Fig. 3b). HRTEM image (Fig. 3b) reveals lattice fringes along (015) of the rhombohedral  $\text{Bi}_2\text{Te}_3$  structure. The SAED pattern shown in inset Fig. 3b confirms a rhombohedral  $\text{Bi}_2\text{Te}_3$  structure with zone axis [001].

### 3.2 Electronic transport properties

Figure 4a–c displays temperature-dependent electrical conductivity, Seebeck coefficient, and calculated power factor. Temperature-dependent electrical conductivity;  $\sigma$  of  $\text{Bi}_{0.5}\text{Sb}_{1.35}\text{Ni}_{0.15}\text{Te}_3$  (Fig. 4a) reveals that  $\sigma$  decreases with increasing temperature indicating metallic in nature. Regardless of temperature, the electrical conductivity of bulk  $\text{Bi}_{0.5}\text{Sb}_{1.35}\text{Ni}_{0.15}\text{Te}_3$  single crystal exhibits  $\sim 1584$  S/cm at 313 K which is much higher than that of bulk single-crystal  $\text{Bi}_{0.5}\text{Sb}_{1.5}\text{Te}_3$  ( $\sigma \sim 400$  S/cm at 313 K) as reported by Drašar et al. [32]. The increased electrical conductivity is ascribed to enhanced carrier concentration due to the substitution of Ni on the Sb site as Ni has fewer electrons in outermost orbital than the Bi and Sb. The carrier concentration of pristine  $\text{Bi}_{0.5}\text{Sb}_{1.5}\text{Te}_3$  and single-crystal  $\text{Bi}_{0.5}\text{Sb}_{1.35}\text{Ni}_{0.15}\text{Te}_3$  is presented in Table 2. With increasing temperature, the decrease of electrical conductivity of  $\text{Bi}_{0.5}\text{Sb}_{1.35}\text{Ni}_{0.15}\text{Te}_3$  may be attributed to low mobility of charge carriers due to pairing of the hole and electron caused by minor charge excitation and also due to hole–electron hopping with small

polaron (lattice distortion) at elevated temperature similar to other report [31].

The carrier concentration of pristine  $\text{Bi}_{0.5}\text{Sb}_{1.5}\text{Te}_3$  and single-crystal  $\text{Bi}_{0.5}\text{Sb}_{1.35}\text{Ni}_{0.15}\text{Te}_3$  is presented in Table 2. Figure 4b represents the Seebeck coefficient of  $\text{Bi}_{0.5}\text{Sb}_{1.35}\text{Ni}_{0.15}\text{Te}_3$  single crystal with increasing temperature. The single crystal of  $\text{Bi}_{0.5}\text{Sb}_{1.35}\text{Ni}_{0.15}\text{Te}_3$  exhibits the positive value of the Seebeck coefficient in the entire temperature suggesting holes to be a majority charge carriers. The Temperature-dependent Seebeck coefficient reveals that the Seebeck coefficient increases with increasing temperature as expected by the Mott equation [33]. However, the Seebeck coefficient of its single crystal of  $\text{Bi}_{0.5}\text{Sb}_{1.35}\text{Ni}_{0.15}\text{Te}_3$  was found to be decreased when compared to that of bare bulk commercial composition  $\text{Bi}_{0.5}\text{Sb}_{1.5}\text{Te}_3$ . The decrease in Seebeck coefficient of  $\text{Bi}_{0.5}\text{Sb}_{1.35}\text{Ni}_{0.15}\text{Te}_3$  ( $\alpha = 105$   $\mu\text{V}/\text{K}$  at 413 K) from commercial composition  $\text{Bi}_{0.5}\text{Sb}_{1.5}\text{Te}_3$  ( $\alpha = 200$   $\mu\text{V}/\text{K}$  at 413 K) can be understood by using a transport equation for degenerated semiconductor [33]:

$$\alpha = \frac{8\pi^2 K^2 m^* T}{3eh^2} \left(\frac{\pi}{3n}\right)^{2/3}$$

where  $K$  is Boltzmann constant,  $h$  is Planck constant,  $m^*$  is effective mass, and  $n$  is carrier concentration.

One can clearly notice from the above equation that the Seebeck coefficient is inversely proportional to  $n^{2/3}$  of carrier concentration on keeping  $m^*$  and  $T$  constant. Thus, reduction of Seebeck coefficient of  $\text{Bi}_{0.5}\text{Sb}_{1.35}\text{Ni}_{0.15}\text{Te}_3$  (105  $\mu\text{V}/\text{K}$  at 413 K) single crystal from the commercial composition  $\text{Bi}_{0.5}\text{Sb}_{1.5}\text{Te}_3$  (200  $\mu\text{V}/\text{K}$  at 413 K) is a result of increased carrier concentration occurred due to doping of Ni in  $\text{Bi}_{0.5}\text{Sb}_{1.5}\text{Te}_3$  as explained above. In addition to this, one can clearly notice the discontinuity and change in the slope of the temperature-dependent Seebeck coefficient (Fig. 4b) which

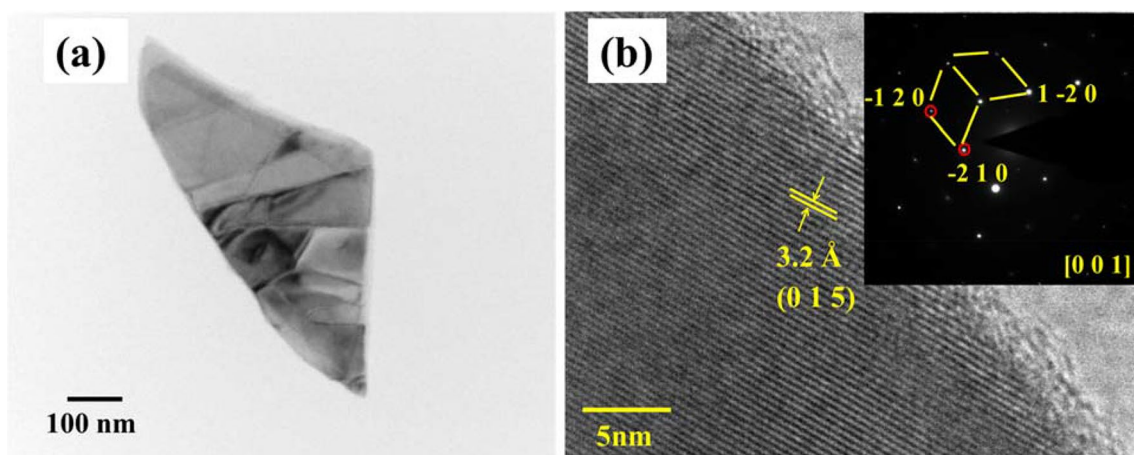


**Fig. 3** **a** Bright-field TEM image and **b** HRTEM image with corresponding SAED (inset **b**) pattern of  $\text{Bi}_{0.5}\text{Sb}_{1.35}\text{Ni}_{0.15}\text{Te}_3$

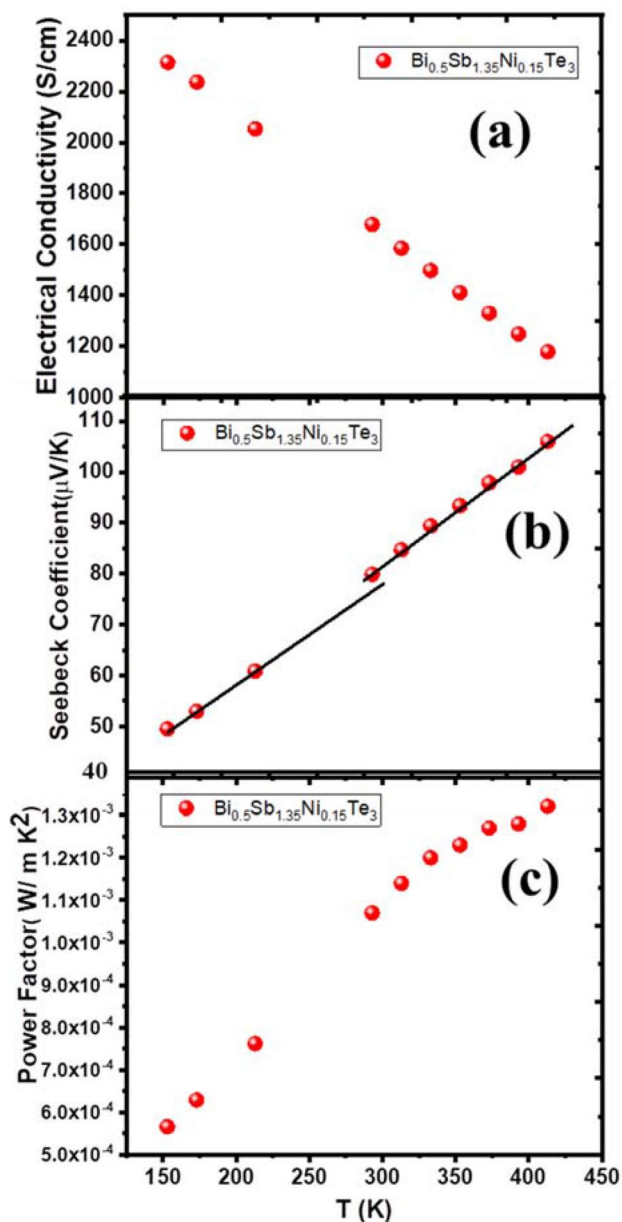


**Fig. 4** Temperature-dependent **a** electrical conductivity, **b** Seebeck coefficient, and **c** estimated power factor of  $\text{Bi}_{0.5}\text{Sb}_{1.35}\text{Ni}_{0.15}\text{Te}_3$

reflects the occurrence of ferromagnetic–paramagnetic transitions at 300 K. This anomalous behavior of the temperature-dependent Seebeck coefficient for  $\text{Bi}_{0.5}\text{Sb}_{1.35}\text{Ni}_{0.15}\text{Te}_3$  is consistent with magnetic behavior discussed in the forthcoming section. As expected, a higher value of the Seebeck coefficient is observed in the paramagnetic region above 300 K, which is possibly due to Ni 3d states lying at  $E_f$  and splitting of Ni 3d band away from a ferromagnetic region similar to an observation in a recent report [20].

The calculated power factor ( $\alpha^2\sigma$ ) with increasing temperature is presented in the Fig. 4c. A large power factor

( $1.32 \times 10^{-3} \text{ W/m K}^2$ ) of  $\text{Bi}_{0.5}\text{Sb}_{1.35}\text{Ni}_{0.15}\text{Te}_3$  at 413 K is achieved which is 20% larger than that of very recently Cr-doped  $\text{Bi}_2\text{Te}_3$  ( $1.1 \times 10^{-3} \text{ W/m K}^2$  at 413 K) [20] and 163% larger than bare single-crystal  $\text{Bi}_{0.5}\text{Sb}_{1.5}\text{Te}_3$  ( $0.63 \times 10^{-3} \text{ W/m K}^2$  at 300 K) as reported by Drašar et al. [32]. The enhanced power factor of present material makes it a potential thermoelectric material.

### 3.3 Magnetic properties

Magnetic dopant Ni-doped in  $\text{Bi}_{0.5}\text{Sb}_{1.5}\text{Te}_3$  provides us an impetus to investigate the magnetic properties of  $\text{Bi}_{0.5}\text{Sb}_{1.35}\text{Ni}_{0.15}\text{Te}_3$  single crystal. Figure 5a presents the magnetization behavior of  $\text{Bi}_{0.5}\text{Sb}_{1.35}\text{Ni}_{0.15}\text{Te}_3$ , which exhibits ferromagnetic ordering. Fluctuations in the magnetization observed in Fig. 5a could be attributed to the other non-magnetic elements present in the sample of  $\text{Bi}_{0.5}\text{Sb}_{1.35}\text{Ni}_{0.15}\text{Te}_3$  single crystal. The paramagnetic transition temperature (Curie temperature)  $T_C$  could be estimated by extending the M-T curve, which may occur above the room temperature. Interestingly, the ferromagnetic ordering of present crystal was observed up to 300 K (Fig. 5a), which is higher than the temperature reported for Mn or Fe-doped  $\text{Bi}_2\text{Te}_3$  (all below 50 K) [34–37]. Further, we have investigated magnetization behavior at 300 K with varying magnetic fields up to 1 T, as shown in Fig. 5b. The magnetization gets saturated around the 0.5 T field. Ferromagnetic alignment of Ni in  $\text{Bi}_{0.5}\text{Sb}_{1.35}\text{Ni}_{0.15}\text{Te}_3$  is also confirmed by observed hysteresis loop (Fig. 5b). From this investigation, it is believed that the improved ferromagnetic components of  $\text{Bi}_{0.5}\text{Sb}_{1.35}\text{Ni}_{0.15}\text{Te}_3$  crystal at a higher temperature may have applications in the field of topological insulators.

### 3.4 Photoluminescence analyses

In the process of investigating the functionality of  $\text{Bi}_{0.5}\text{Sb}_{1.35}\text{Ni}_{0.15}\text{Te}_3$  single crystal, we have also examined the optical properties of this crystal by measuring emission spectra employing photoluminescence (PL) spectroscopy. Generally, the PL technique is used to study the active surface sites of materials. It gives information regarding the recombination of electron–hole, surface defect, oxygen vacancy, and phase formation of materials [38–40]. Here, the sample was excited at room temperature with a pump of a laser of 375 nm. The PL emission spectra is shown in Fig. 6 which indicates a strong peak of red emission at  $\sim 612 \text{ nm}$  and can be attributed to the fast recombination rate of photo-generated charges [40]. The optical bandgap  $\sim 2.1 \text{ eV}$  for  $\text{Bi}_{0.5}\text{Sb}_{1.35}\text{Ni}_{0.15}\text{Te}_3$  single crystal was estimated corresponding to red emission peak. In addition to this, the intensity peak of  $\text{Bi}_{0.5}\text{Sb}_{1.35}\text{Ni}_{0.15}\text{Te}_3$  is found to be increased from pristine  $\text{Bi}_{0.5}\text{Sb}_{1.5}\text{Te}_3$ , which reflects increased charge

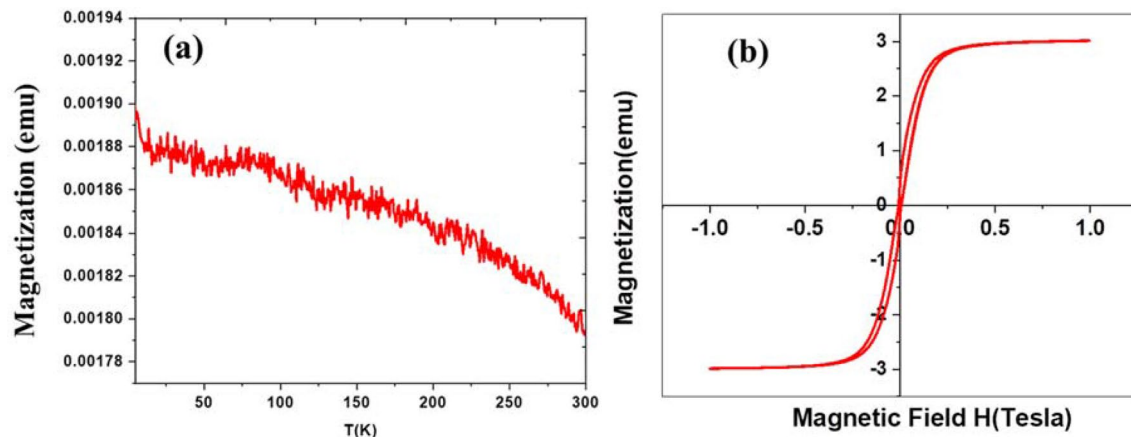


**Fig. 5** **a** Temperature dependence magnetization and **b**  $M$ - $H$  curve of  $\text{Bi}_{0.5}\text{Sb}_{1.35}\text{Ni}_{0.15}\text{Te}_3$  at 300 K

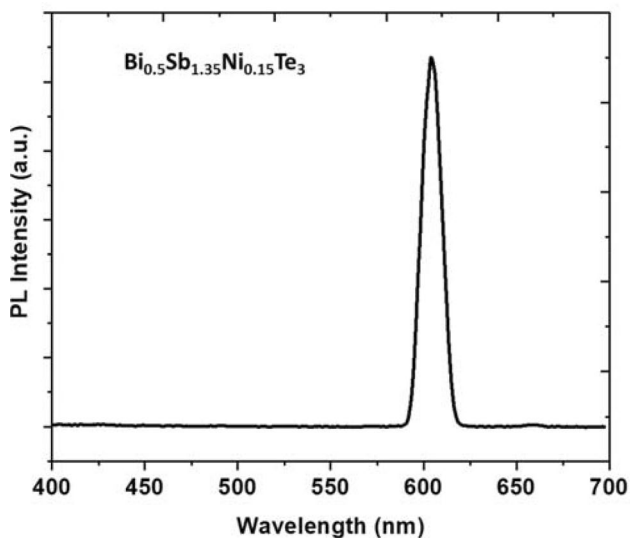


**Fig. 6** PL emission spectra obtained for  $\text{Bi}_{0.5}\text{Sb}_{1.35}\text{Ni}_{0.15}\text{Te}_3$

carrier's recombination in  $\text{Bi}_{0.5}\text{Sb}_{1.35}\text{Ni}_{0.15}\text{Te}_3$  as observed in other report [40]. It is expected that such a large optical bandgap of the present sample makes it a potential candidate for numerous applications in the field of optoelectronics [15, 16] if studied by using various magnetic dopants.

## 4 Conclusion

The single-crystal  $\text{Bi}_{0.5}\text{Sb}_{1.35}\text{Ni}_{0.15}\text{Te}_3$  was successfully grown by the self-flux method via solid-state reaction. The single-crystal growth leads to significantly increased electrical conductivity (1177 S/cm at 413 K) in this class of thermoelectric materials without much affecting the Seebeck coefficient. Significantly increased electrical conductivity results in an enhanced power factor. This enhanced

power factor  $\sim 1.32 \times 10^{-3} \text{ W/m K}^2$  of  $\text{Bi}_{0.5}\text{Sb}_{1.35}\text{Ni}_{0.15}\text{Te}_3$  at 413 K is observed to be 20% larger than that of very recently Cr-doped  $\text{Bi}_2\text{Te}_3$  (p.f. =  $1.1 \times 10^{-3} \text{ W/m K}^2$  at 413 K) material. Magnetic doping of Ni in  $\text{Bi}_{0.5}\text{Sb}_{1.5}\text{Te}_3$  and developing single crystal as investigated in the present work stands to be a reasonably efficient strategy to achieve a high power factor of thermoelectric materials for its enhanced efficiency. Further, observed ferromagnetic behavior at a temperature higher than 200 K for  $\text{Bi}_{0.5}\text{Sb}_{1.35}\text{Ni}_{0.15}\text{Te}_3$  single-crystal manifests new insights to the field of topological insulators. The functionality of a single crystal of  $\text{Bi}_{0.5}\text{Sb}_{1.35}\text{Ni}_{0.15}\text{Te}_3$  is also examined in terms of optical properties. Interestingly, such a magnetically doped single crystal examined by photoluminescence (PL) spectroscopy reveals a large optical bandgap  $\sim 2.1 \text{ eV}$  for  $\text{Bi}_{0.5}\text{Sb}_{1.35}\text{Ni}_{0.15}\text{Te}_3$  which makes it a potential candidate for numerous applications in the field of optoelectronics.

**Acknowledgements** Authors highly acknowledge Dr. Aman Bhardwaj for magnetic measurement, Dr. Anupama Singh and Mr. Hemant Sharma for TE measurements, Dr. N. Vijayan for guiding in growing the single crystal, and Mr. Praveen Tanwar for carrying out the PL measurement. One of the authors, SB, greatly acknowledges financial support from UGC.

## Compliance with ethical standards

**Conflict of interest** The authors declare that they have no known competing for financial interests or personal relationships that could have appeared to influence the work reported in this paper.

## References

- G.J. Snyder, E.S. Toberer, in *Mater. Sustain. Energy a Collect. Peer-Reviewed Res. Rev. Artic. from Nat. Publ. Gr.* (World Scientific, 2011), pp. 101–110
- H. Wang, Y. Pei, A.D. LaLonde, G.J. Snyder, *Adv. Mater.* **23**, 1366 (2011)
- Y. Lee, S.-H. Lo, J. Androulakis, C.-I. Wu, L.-D. Zhao, D.-Y. Chung, T.P. Hogan, V.P. Dravid, M.G. Kanatzidis, *J. Am. Chem. Soc.* **135**, 5152 (2013)
- K. Ahn, K. Biswas, J. He, I. Chung, V. Dravid, M.G. Kanatzidis, *Energy Environ. Sci.* **6**, 1529 (2013)
- Y. Pei, H. Wang, Z.M. Gibbs, A.D. LaLonde, G.J. Snyder, *NPG Asia Mater.* **4**, e28 (2012)
- L.M. Rogers, A.J. Crocker, *J. Phys. D Appl. Phys.* **4**, 1016 (1971)
- S.A. Yamini, H. Wang, Z.M. Gibbs, Y. Pei, S.X. Dou, G.J. Snyder, *Phys. Chem. Chem. Phys.* **16**, 1835 (2014)
- J.P. Heremans, V. Jovovic, E.S. Toberer, A. Saramat, K. Kurosaki, A. Charoenphakdee, S. Yamanaka, G.J. Snyder, *Science* (80-). **321**, 554 (2008)
- R. Basu, S. Bhattacharya, R. Bhatt, M. Roy, S. Ahmad, A. Singh, M. Navaneethan, Y. Hayakawa, D.K. Aswal, S.K. Gupta, *J. Mater. Chem. A* **2**, 6922 (2014)
- N. Tsujii, T. Mori, *Appl. Phys. Express* **6**, 43001 (2013)
- R. Ang, A.U. Khan, N. Tsujii, K. Takai, R. Nakamura, T. Mori, *Angew. Chemie Int. Ed.* **54**, 12909 (2015)
- F. Ahmed, N. Tsujii, T. Mori, *J. Mater. Chem. A* **5**, 7545 (2017)
- N. Tsujii, A. Nishide, J. Hayakawa, T. Mori, *Sci. Adv.* **5**, eaat5935 (2019)
- M. Zhao, J. Zhang, N. Gao, P. Song, M. Bosman, B. Peng, B. Sun, C. Qiu, Q. Xu, Q. Bao, *Adv. Mater.* **28**, 3138 (2016)
- P. Sharma, M.M. Sharma, M. Kumar, V.P.S. Awana, *Solid State Commun.* **319**, 114005 (2020)
- P. Sharma, M. Kumar, V.P.S. Awana, *J. Mater. Sci. Mater. Electron.* **31**, 7959 (2020)
- T.M. Tritt, D.M. Rowe, *Thermoelectric Handbook: Macro to Nano* (2005)
- H. Qin, Y. Liu, Z. Zhang, Y. Wang, J. Cao, W. Cai, Q. Zhang, J. Sui, *Mater. Today Phys.* **6**, 31 (2018)
- X.T. Dai, Y. Yu, F.Q. Zu, Z.Y. Huang, *Mater. Sci. Forum* **847**, 177 (2016)
- J.B. Vaney, S. Aminorroaya Yamini, H. Takaki, K. Kobayashi, N. Kobayashi, T. Mori, *Mater. Today Phys.* **9**, 100090 (2019)
- W. Hu, T. Li, X. Liu, D. Dastan, K. Ji, P. Zhao, *J. Alloys Compd.* **818**, 152933 (2020)
- K. Shan, Z.Z. Yi, X.T. Yin, D. Dastan, H. Garmestani, *Dalt. Trans.* **49**, 6682 (2020)
- G. Awana, R. Sultana, P.K. Maheshwari, R. Goyal, B. Gahtori, A. Gupta, V.P.S. Awana, *J. Supercond. Nov. Magn.* **30**, 853 (2017)
- D. Dastan, *Appl. Phys. A Mater. Sci. Process.* **123**, 0 (2017)
- W.D. Zhou, D. Dastan, J. Li, X.T. Yin, Q. Wang, *Nanomaterials* **10**, 785 (2020)
- A. Jafari, M.H. Alam, D. Dastan, S. Ziakhodadadian, Z. Shi, H. Garmestani, A.S. Weidenbach, Ş Tǎlu, *J. Mater. Sci. Mater. Electron.* **30**, 21185 (2019)
- A. Jafari, K. Tahani, D. Dastan, S. Asgary, Z. Shi, X.T. Yin, W.D. Zhou, H. Garmestani, Ş Tǎlu, *Surf. Interfaces* **18**, 100463 (2020)
- D. Dastan, S.L. Panahi, N.B. Chaure, *J. Mater. Sci. Mater. Electron.* **27**, 12291 (2016)
- F. Serrano-Sánchez, M. Gharsallah, N.M. Nemes, N. Biskup, M. Varela, J.L. Martínez, M.T. Fernández-Díaz, J.A. Alonso, *Sci. Rep.* **7**, 1 (2017)
- P. Lu, L. Chen, H. Chen, F. Hao, D. Ren, Q. Song, P. Qiu, X. Shi, *Materials (Basel)*. **10**, 251 (2017)
- K. Shan, Z.-Z. Yi, X.-T. Yin, D. Dastan, H. Garmestani, *Dalt. Trans.* (2020). <https://doi.org/10.1039/D0DT02345K>
- Č Drašar, A. Hovorková, P. Lošt'ák, H. Kong, C.P. Li, C. Uher, *J. Appl. Phys.* **104**, 2 (2008)
- V.A. Johnson, K. Lark-Horovitz, *Phys. Rev.* **92**, 226 (1953)
- J. Choi, S. Choi, J. Choi, Y. Park, H. Park, H. Lee, B. Woo, S. Cho, *Phys. Status Solidi* **241**, 1541 (2004)
- Z. Zhou, C. Uher, M. Zabcik, P. Lostak, *Appl. Phys. Lett.* **88**, 192502 (2006)
- N.H. Jo, K.J. Lee, C.M. Kim, K. Okamoto, A. Kimura, K. Miyamoto, T. Okuda, Y.K. Kim, Z. Lee, T. Onimaru, *Phys. Rev. B* **87**, 201105 (2013)
- J.S. Lee, A. Richardella, D.W. Rench, R.D. Fraleigh, T.C. Flanagan, J.A. Borchers, J. Tao, N. Samarth, *Phys. Rev. B* **89**, 174425 (2014)
- D. Dastan, P.U. Londhe, N.B. Chaure, *J. Mater. Sci. Mater. Electron.* **25**, 3473 (2014)
- D. Dastan, N. Chaure, M. Kartha, *J. Mater. Sci. Mater. Electron.* **28**, 7784 (2017)
- X.T. Yin, D. Dastan, F.Y. Wu, J. Li, *Nanomaterials* **9**, 1 (2019)

**Publisher's Note** Springer Nature remains neutral with regard to jurisdictional claims in published maps and institutional affiliations.